Accepted Manuscript

NANO

Article Title:	Nitrogen and fluorine dual-doped carbon nanosheets for high performance supercapacitors
Author(s):	Chen Jiao, Zhong Jie Zhang, Xiang Ying Chen
DOI:	10.1142/S1793292019500425
Received:	01 November 2018
Accepted:	25 February 2019
To be cited as:	Chen Jiao, Zhong Jie Zhang, Xiang Ying Chen, Nitrogen and fluorine dual-doped carbon nanosheets for high performance supercapacitors, *NANO*, doi: 10.1142/S1793292019500425
Link to final version:	https://doi.org/10.1142/S1793292019500425

World Scientific
www.worldscientific.com

Nitrogen and fluorine dual-doped carbon nanosheets for high performance supercapacitors

Chen Jiao[1,2], Zhong Jie Zhang[3,*], and Xiang Ying Chen[4]

[1]*State Key Laboratory of Luminescence and Applications Changchun Institute of Optics, Fine Mechanics and Physics Chinese Academy of Sciences No. 3888 Dongnanhu Road, Changchun 130033, P. R. China. Email: george13200@126.com.*

[2]*University of Chinese Academy of Sciences Beijing 100049, P. R. China.*

[3]*School of Chemistry & Chemical Engineering, Anhui Province Key Laboratory of Environment-friendly Polymer Materials, Anhui University, Hefei 230601, Anhui, P. R. China. * The corresponding author. E-mail: zhangzj0603@126.com.*

[4]*School of Chemistry and Chemical Engineering, Anhui Key Laboratory of Controllable Chemistry Reaction & Material Chemical Engineering, Hefei University of Technology, Hefei, Anhui 230009, P. R. China. E-mail: chenxy@hfut.edu.cn.*

Abstract

Doping carbon materials with heteroatoms such N, F is an effective approach to elevating the capacitive performance of supercapacitors. In this work, nitrogen and fluorine dual-doped two-dimensional (2D) porous carbon nanosheets (PCNSs) have been fabricated by a straightforward template carbonization method, using trisodium citrate as carbon source and self-template, and ammonium fluoride as N/F dopants. The N/F-doped carbon samples are well characterized by a series of techniques and measured in a three-electrode system and two-electrode system, respectively. As a result, N/F-doped carbon has delivered large capacitance of 110 F g^{-1} at 1A g^{-1} and high energy density of 3.82 W h kg^{-1} at the power density of 0.5 kW kg^{-1}. It is also revealed that semi-ionic C–F bonds in PCNSs have enhanced electrical conductivity, hence facilitating electron transport in the electrode. For comparison, ammonium chloride is used as sole dopant for producing N-doped carbon materials, whose capacitive performances are much lower than the N/F-codoped one, indicating the synergistic effect of N/F for capacitive improvement.

Keywords: Carbon nanosheets; Dopant; Nitrogen; Fluorine; Supercapacitor.

1. Introduction

Two-dimensional (2D) porous carbon nanosheets (PCNSs), compared with traditional porous carbon materials, have shown many scientific advantages of faster ion/electron transfer, shorter ion/electron transport/diffusion length and higher charge-induced ion-adsorbing surface area,[1] which are very likely to serve as electrode materials for high performance supercapacitors.[2,3] So far, many routes have been developed to synthesize PCNSs, mainly including chemical vapor deposition (CVD), solvothermal synthesis, chemical or physical exfoliation, templating, and self-assembly.[4] Among these, templating method (more commonly called as template carbonization method) is proved to be a powerful tool for producing carbon materials, primarily showing precisely controlled structures at the nanometer level.[5] For example, large scale PCNSs have been successively fabricated through the above strategy, using different kinds of carbon sources and templates such as 1,5-diphenylcarbazide and $MgCl_2 \cdot 6H_2O$,[6] thiocarbanilide and $Mg(OH)_2$,[7] and sodium stearate and magnesium,[8] respectively. Furthermore, it is notable for us that the production of PCNSs with large areas has been implemented for these cases, and nevertheless it remains the troublesome post treatment of templates additionally added. In brief, to explore a simpler template carbonization method, especially without the use of extra template, seems to be intriguing for PCNSs synthesis.

For achieving high performance supercapacitors, one imperative way is to accurately control the intrinsic pore structures of PCNSs, and another alternative one is the doping of hetero-atoms (N, B, P, S, F *etc*.) within carbon matrix, which could largely adjust physical properties of carbon materials, including conductivity and wettability.[9] As far as ubiquitous nitrogen is concerned, it indicates more electron-rich and polar in contrast to that of carbon, which thereby leads to increased electrical conductivity and better wettability.[10-12] In addition, another useful heteroatom is fluorine, also quite improving pseudo-capacitance, which acts as the similar functionality to that of N atom. It reveals that F-doping and the large interlayer distance as well as the disorder structure contributes to a lowering of the sodium ion insertion–extraction barrier, thus promoting the Na^+ diffusion and providing more active sites for Na^+ storage.[13]

With the development of supercapacitor electrode materials, it has recently reached a consensus that doping two or more types of heteroatoms into carbon matrix

can further enhance the capacitive performance on account of the synergistic effects among the doped species.[14-16] For instance, Gao et al. reported ultrahigh volumetric capacitance of 521 F cm^{-3} in aqueous electrolytes for non-porous carbon microsphere electrodes co-doped with fluorine and nitrogen;[17] Nitrogen and fluorine doped mesoporous carbon nanofibers (NFMCNFs) were fabricated using a hydrothermal treatment for structural modification to create porosity and a vacuum plasma process for introducing heteroatoms into the carbon lattice. Applied to supercapacitor devices, the NFMCNFs exhibited a remarkable EDLC performance of 252.6 F g^{-1} at 0.5 A g^{-1} in a 1 M H_2SO_4 electrolyte;[18] N, F co-doped activated carbon (ACNF) was successfully prepared by a microwave-assisted hydrothermal method, utilizing commercial activated carbon (ACR) as the precursor and ammonium tetrafluoroborate as the single source. The rate capability was higher compared to that of raw activated carbon because N and F codoping increased the electrical conductivity of AC-NF.[19] Yet, as given above, both complicated apparatus and rigorous fluorine source such as hydrofluoric acid or octafluorocyclobutane (C_4F_8) gas has greatly restricted the fluorination of carbon materials, and thereby how to find out a milder synthesis approach to realizing effective nitrogenation/fluorination towards carbons is still challenging.

Herein, we used trisodium citrate dihydrate as carbon source and ammonium chloride & ammonium fluoride as nitrogen/fluorine source, respectively, by a straightforward template carbonization method to produce N-doped or N/F dual-doped carbon materials. The as-obtained carbon samples were fully characterized by a series of techniques including XRD, Raman, XPS, BET&PSD and HRTEM. Finally, the corresponding capacitive behaviors were measured in a three-electrode system and two-electrode system, respectively.

2. Experimental section

Aiming to fabricate 2D PCNSs doped with nitrogen and/or fluorine species, in present work, we adopted trisodium citrate dihydrate as carbon source and ammonium chloride & ammonium fluoride as special dopants. The above considerations are based on the following reasons: firstly, due to the scientific advantages of 2D carbon nanostructures compared to irregular porous carbon materials, the research target is to produce 2D carbon nanosheets and trisodium citrate dihydrate was chosen as carbon precursor, mainly because it can thermally

decompose into carbon nanosheets when simply being heated at elevated temperatures;[20] secondly, in order to realize the doping of carbon matrix with nitrogen and/or fluorine species, we used ammonium chloride and ammonium fluoride as dopants when being heated with trisodium citrate dihydrate.

Note that the possible formation mechanism for producing 2D carbon nanostructures derived from the pyrolysis of trisodium citrate dihydrate can be illustrated as follows: As reported previously, trisodium citrate dihydrate loses two water molecules at 160 °C, and then the generated trisodium citrate further decomposes (>295 °C) to produce carbon, coexistent with gases and sodium carbonate.[20] In particular, the freshly synthesized sodium carbonate play an crucial role in determining the formation of 2D carbon nanostructures, as the inorganic Na_2CO_3 salt could enhance the dehydration and crosslinking reactions and increases the carbon yield.[21]

For the case of trisodium citrate dihydrate and ammonium chloride, a synchronous carbonization and nitrogenation process occurs at elevated temperatures, in which the freshly produced ammonia gas (coming from the decomposition of ammonium chloride) will be incorporated into carbon materials (stemming from the carbonization of trisodium citrate dihydrate), eventually achieving the N-doped carbon materials; besides, as for the case of trisodium citrate dihydrate and ammonium fluoride, in a similar manner, N/F dual-doped carbon materials come into being via a synchronous carbonization and nitrogenation/fluorination process.

Additionally, what is worth paying attention to is the doping ability of halogen elements, and evidently the atomic radius is a key effect to be considered. As a result, nitrogen and fluorine with atomic radii of 65 and 50 pm respectively to large extent match with carbon atom (that of 70 pm); however, chlorine element (100 pm) is nonequivalent to that of carbon atom owing to the large radii discrepancy. As a consequence, nitrogen and/or fluorine could be feasibly incorporated into carbon matrix whilst chlorine is not preferrable.

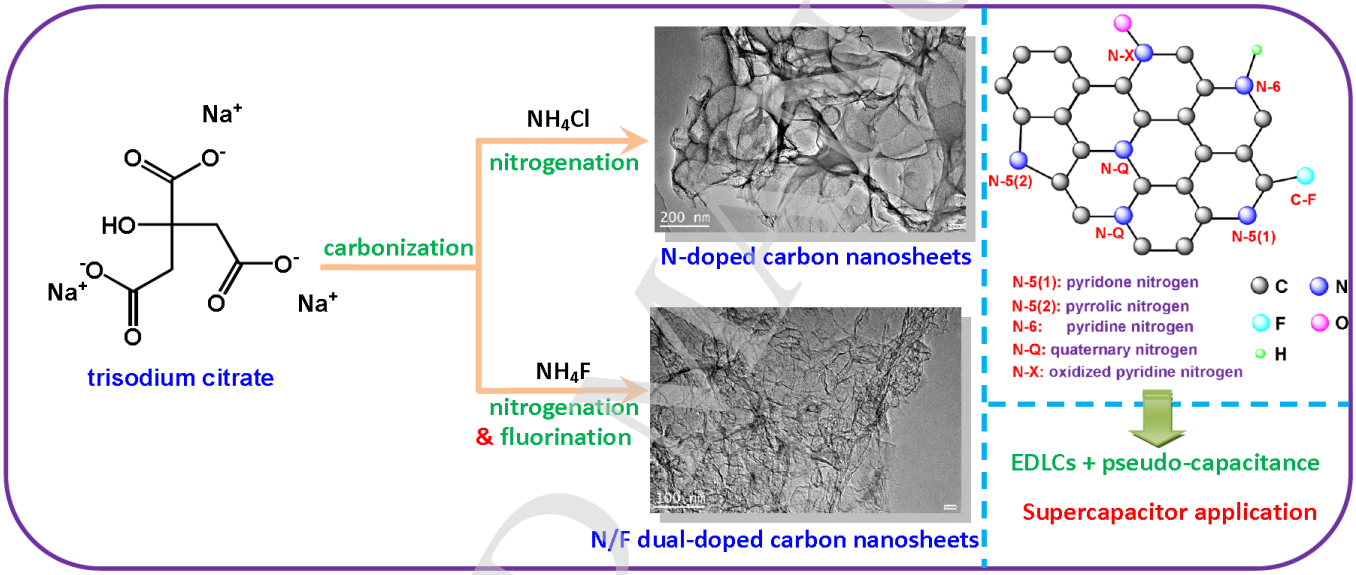

Figure 1. Schematic diagram of the synthesis procedure for carbon nanosheets doped with N/F as well as structural formula of nitrogen/fluorine groups in a graphitic structure.

2.1 Typical procedure for synthesizing the carbon-N-F sample

All the chemicals are of analytical grade, coming from Sinopharm Chemical Reagent Co. Ltd, and used as received without further purification.

Typically, certain amount of trisodium citrate dihydrate ($C_6H_5Na_3O_7 \cdot 2H_2O$) and ammonium fluoride (NH_4F) with the mass ratio of 1:2 were firstly milled in a mortar about 10 min and then transferred into a porcelain boat. After flowing with N_2 for 30 min, it was further heated up to 800 °C at a rate of 4 °C min^{-1} and maintained for 2h under N_2 flow in a horizontal tube furnace. After that, the product was immersed in diluted HCl solution (1 mol L^{-1}) for 4 h. Subsequently, the products were washed with deionized water, until the pH of filtrate to be 7. Finally, the filtered product was dried in vacuum at 110 °C for 12 h, obtaining the ***carbon-N-F*** sample.

As for the ***carbon-blank*** sample, it was obtained by solely carbonizing trisodium citrate dihydrate, maintaining the other reaction conditions unchanged; and the ***carbon-N*** sample was synthesized by trisodium citrate dihydrate and ammonium chloride (NH_4Cl) with the mass ratio of 1:2 while keeping other parameters invariable.

2.2 Structure characterization

The visualized morphology of the carbon sample was characterized by field emission scanning electron microscopy (FESEM; Hitachi S-4800, operated at a voltage of 10 kV). High-resolution transmission electron microscope (HRTEM) images, elemental mappings and EDAX spectrum were performed with a JEM-2100F unit. X-ray diffraction (XRD) pattern was obtained on a Rigaku D/MAX2500V with Cu Kα radiation. Raman spectrum was recorded at ambient temperature on a Spex 1403 Raman spectrometer with an argon-ion laser at an excitation wavelength of 514.5 nm. The specific surface area and pore structure of the carbon sample were determined by N_2 adsorption-desorption isotherms at 77 K (Quantachrome Autosorb-iQ). The specific surface area was calculated by the BET (Brunauer-Emmett-Teller) method. Pore size distribution was calculated by using a slit/cylindrical nonlocal density functional theory (NLDFT) model. X-ray photoelectron spectra (XPS) were obtained using a VG Instruments ESCALAB MK II X-ray photoelectron spectrometer with an excitation source of Al Ka (1486.6 eV).

2.3 Electrochemical measurements conducted in a three-electrode system

Typically, the carbon sample (80wt%), graphite (15wt%) and polytetrafluoroethylene (5wt%) were mixed in ethanol. The mixed slurry (active carbon materials of 3~4 mg) was coated onto platinum net (~ 1 cm^2) to prepare the working electrode, and the electrode was dried at 110 °C in an oven for 12 h.The three electrode system was executed in the prepared electrolyte (6 mol L^{-1} KOH solution) with a counter electrode of platinum foil (6 cm^2) and a reference electrode of saturated calomel electrode (SCE). All texts were carried out on a CHI 760E (Chen Hua Instruments Co. Ltd., Shanghai). The electrochemical performances of the samples were evaluated by cyclic voltammetry (CV), galvanostatic charge-discharge (GCD), and electrochemical impedance spectroscopy (EIS) techniques. The EIS measurements were carried out in the frequency range from 100 kHz to 0.01 Hz at open circuit potential with an ac perturbation of 5 mV.

Specific capacitances derived from galvanostatic tests can be calculated from the equation:

$$C = \frac{Idt}{mdU} \tag{1}$$

Where C (F g^{-1}) is the specific capacitance; I (A) is the discharge current; t (s) is the discharge time; U (V) is the potential; and m (g) is the mass of active materials loaded in working electrode.

Energy efficiency (η_E) was calculated using the equation:

$$\eta_E = \frac{\Delta t_{\mathrm{int}/d}}{\Delta t_{\mathrm{int}/c}} \tag{2}$$

where $\Delta t_{\mathrm{int/c}}$ and $\Delta t_{\mathrm{int/d}}$ are integral charging and discharging time, respectively.

2.4 Electrochemical measurements conducted in a two-electrode system

The electrochemical experiments in two-electrode system were performed in a CR2032 corn-type cell. The carbon electrode was used as the working electrode and another carbon electrode with the same mass of active material was used as the counter electrode. A glassfiber membrane was used as the separator for the symmetric

supercapacitor. Note that the mass of active carbon materials on each electrode is 1~2 mg.

Specific capacitances derived from galvanostatic tests can be calculated from the equation:

$$C = \frac{2Idt}{mdU} \quad (3)$$

Where I (A) is the constant current; m (g) is the mass of active material loaded on the single electrode; U is the voltage window (V); C (F g^{-1}) is the specific capacitance.

Specific energy density (E) and specific power density (P) derived from galvanostatic tests can be calculated from the equations:

$$E = \frac{1}{3.6} \times \frac{1}{8} \times C\Delta U^2 \quad (4)$$

$$P = \frac{3600E}{\Delta t} \quad (5)$$

E (Wh kg^{-1}) is the energy density; C (F g^{-1}) is the specific capacitance; U (V) is the potential; and P (W kg^{-1}) is the power density and t (h) is the discharge time.

3. Results and discussion

3.1 Structural characterization

X-ray diffraction is usually used to study the structure, composition, and physical properties of materials. In this work, we firstly employed XRD technique to characterize the intrinsic structure of the ***Carbon-blank***, ***Carbon-N-F***, and ***Carbon-N*** samples, and the resulting XRD patterns with 2 theta scope of 10 ~ 90° are displayed in Figure 2a. Apparently, there exists one broad but low-intensity diffraction peak for each sample, centered at ca. 25.1° that corresponds to (002) crystal plane. As we know, the (002) crystal plane is representative for standard graphite and the corresponding 2 theta data is ca. 26.6° in accordance with classic *Bragg Eq.* $2d\sin\theta = \lambda$. It is obvious to us that the present (002) crystal plane has somewhat shifted to left direction, compared to the standard graphite, hence indicating the amorphous or disordered feature of the ***Carbon-blank, Carbon-N-F,*** and ***Carbon-N*** samples. Furthermore, the

enlarged interlayer spacing is believed to be favorable for increasing porosity as well as lowering electrolyte diffusion. As for the ones at ca. 42.6°, they are actually indexed as (100) and (101) planes of standard graphite, which are generally signed as (10) planes primarily due to their contiguous positions.

Next, the authentic structure of the ***Carbon-blank***, ***Carbon-N-F***, and ***Carbon-N*** samples was characterized by Raman tool, because Raman spectrum is particularly sensitive to carbon microstructures, thus providing useful diagnostics for carbon structure and properties.[22] As shown in Figure 2b, c, d, two dissociated peaks are located at 1342.6 and 1594.8 cm^{-1}, respectively, which are definitely indicative of non-graphitic carbon structures.[23] To further illustrate the Raman results, we used Lorentz curve fitting method scoping from 500 to 2000 cm^{-1}, and eventually four peaks with different positions occur. In details, they can be indexed as D and G band (with higher intensities) as well as disordered graphitic lattice and amorphous carbon[24] (with lower intensities), as described in Figure 2b, c, d.

Besides, Tuinstra and Koenig proposed the following *Eq*. 6 to evaluate the graphite cluster size, where I_D/I_G represents the intensity ratio of D and G band; L_a is graphitic in-plane microcrystallite size, and C_λ is ~ 4.4 nm.[25,26]

$$\frac{I_D}{I_G} = \frac{C_\lambda}{L_a} \tag{6}$$

Herein, the I_D/I_G data for the ***Carbon-blank, Carbon-N-F,*** and ***Carbon-N*** samples are tested to be 1.37, 0.99 and 1.03, respectively, and the resulting L_a are of 3.21, 4.44 and 4.27 nm, respectively. It is thus concluded that incorporating N/F species into carbon matrix has to some extent increased the graphitic in-plane microcrystallite size in contrast to the pristine one; and also, the ***Carbon-N-F*** sample has manifested the largest L_a among these samples, principally owing to the synergistic doping of N and F elements.

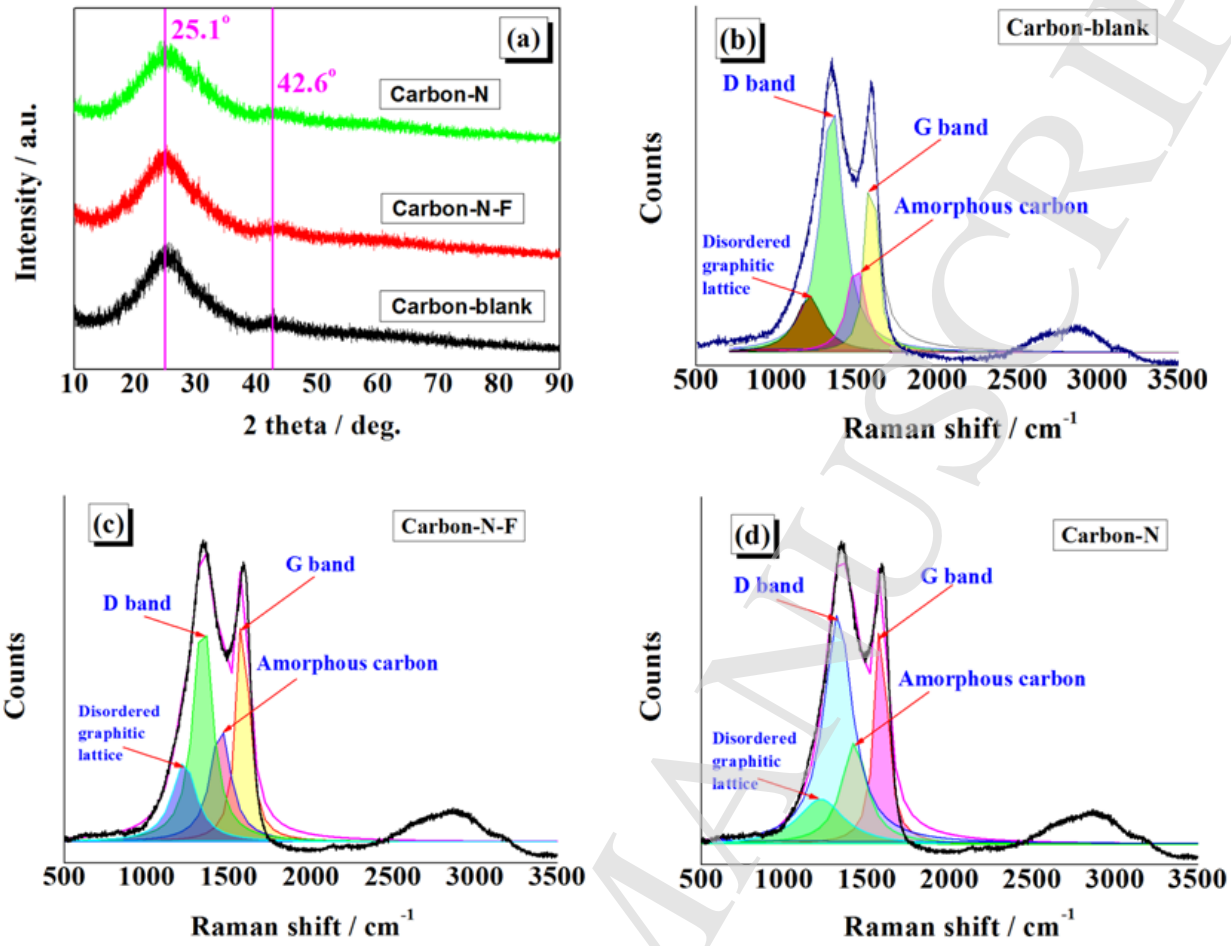

Figure 2. The ***Carbon-blank, Carbon-N-F, Carbon-N*** samples: (a) XRD patterns; (b, c, d) Raman spectra.

Carbon porosity mainly including BET surface area, total pore volume and PSD has significantly influenced the capacitive performance of supercapacitors, and, for example, hierarchical micro-meso-macro porosity improved the rate performance of the biochar-based carbons.[27] In present work, we used N_2 adsorption-desorption technique to investigate the porosity features of the ***Carbon-blank***, ***Carbon-N-F***, and ***Carbon-N*** samples. As depicted in Figure 3 a, b, c, all of the isotherms can be ascribed to type-IV (IUPAC classification) on the basis of the representative hysteresis loops at the pressure scope of 0.45 ~ 1.0. That is to say, the present carbon samples are basically composed of micropores, mesopores and macropores,[28] as also evinced by the PSD curves in Figure 3d. This kind of hierarchical pore structures are clearly favorable of obtaining high performance supercapacitors, in which actual energy storage occurring predominately in smaller micropores whereas larger pores provide fast mass-transport of electrolytes to and from the micropores.[29]

Although the isotherms are almost the same in shapes, their BET surface areas (S_{BET}) and total pore volumes (V_T) largely differentiate from each other. In terms of Table 1, the ***Carbon-blank*** sample exhibits the largest S_{BET} of 1062 m^2 g^{-1} together with the largest V_T of 2.91 cm^3 g^{-1}. However, by incorporating heteroatoms such as N/F, the resulting S_{BET} and V_T have decreased to large extent. As a result, the ***Carbon-N-F*** sample has shown the smallest S_{BET} and V_T of 592 m^2 g^{-1} and 0.84 cm^3 g^{-1}, respectively. This is probably incurred by the fact that the ***Carbon-N-F*** sample possesses the largest graphitic in-plane microcrystallite size (L_a is 4.44 nm), as already illustrated in Figure 2, and this kind of graphitic structure is of course detrimental to optimize/adjust pore structures.

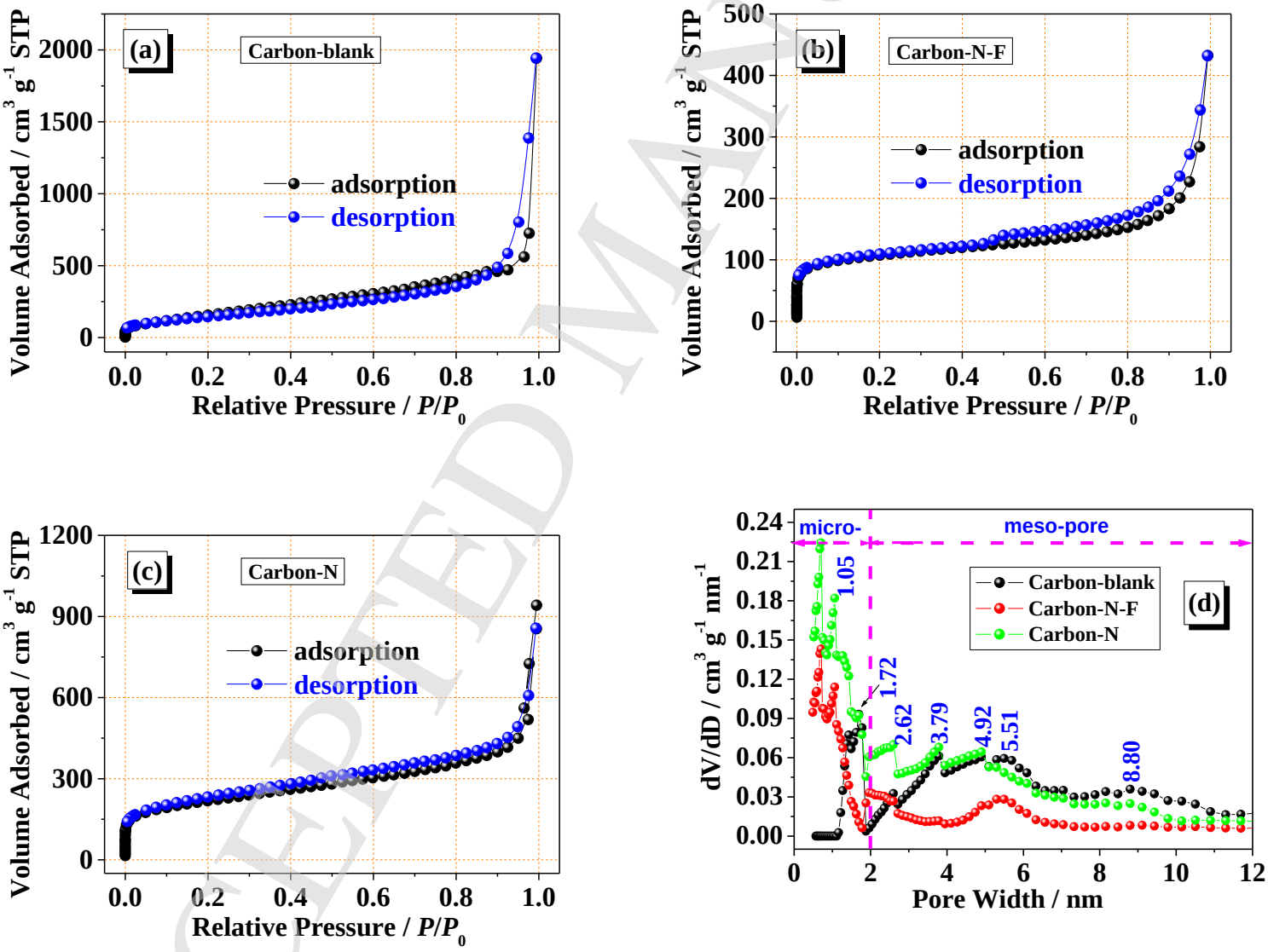

Figure 3. The ***Carbon-blank, Carbon-N-F, Carbon-N*** samples: (a, b, c) N_2 adsorption-desorption isotherms; (d) Pore size distribution curves.

Table 1. Summary of the pore structures of the carbon materials.

samples	BET surface area / m^2 g^{-1}	Total pore volume / cm^3 g^{-1}	Pore width / nm
Carbon-blank	1062	2.91	3.31
Carbon-N-F	592	0.84	3.02
Carbon-N	779	1.04	4.16

XPS is a surface-sensitive quantitative spectroscopic technique that measures the elemental composition, chemical state and electronic state of the elements that exist within a material, and these XPS parameters are quite crucial for determining the capacitive performance of carbon-based supercapacitors.[30] Figure S1 indicates the contrast XPS survey spectra of the ***Carbon-blank***, ***Carbon-N-F***, and ***Carbon-N*** samples, ranging the binding energy from 0 to 1300 eV. To all appearances, the ***Carbon-blank*** sample consists of large amount of C and O elements, whilst the other samples are composed of abundant C, O and N. Regarding the F element within the ***Carbon-N-F*** sample, it is hardly to be detected from the XPS survey spectrum mostly due to the minor content. Next, we employed XPSPEAK software to fit the spectrum of C 1s, N 1s and F 1s in details. Figure 4 a, b, c show the C 1s of the ***Carbon-blank***, ***Carbon-N-F***, and ***Carbon-N*** samples; and also, in the binding energy scope of 280 ~ 297 eV, they can be deconvoluted into five sub-bands. All of them are approximately located at 284.9, 286.3, 287.9, 289.5, and 291.3 eV, and can be assigned to C─C/C═C, C─O, C═O, ─COO, and π─π*, respectively.[23,31,32] Note that the binding energies for C─C (sp^3) and C═C (sp^2) are quite close, and therefore they are represented as a combination of C─C/C═C in present work.

Concerning the ***Carbon-N-F,*** and ***Carbon-N*** samples, their N 1s spectra in Figure 4 d, e can also be fitted into five sub-bands, generally situated at 398.2, 399.8, 400.7, 401.9, and 404.2 eV, which correspond to N-6, N-5, N-Q, N-X and chemisorbed N, respectively. In details, N-6 indicates the pyridine nitrogen; N-5 represents the pyrrolic nitrogen and/or pyridone nitrogen; as for N-Q, it depicts the quaternary nitrogen; N-X indicates the oxidized pyridine nitrogen. [33,34] These nitrogen

functional groups can induce surface redox reactions in aqueous alkaline electrolytes and the possible redox reactions are listed as follows:

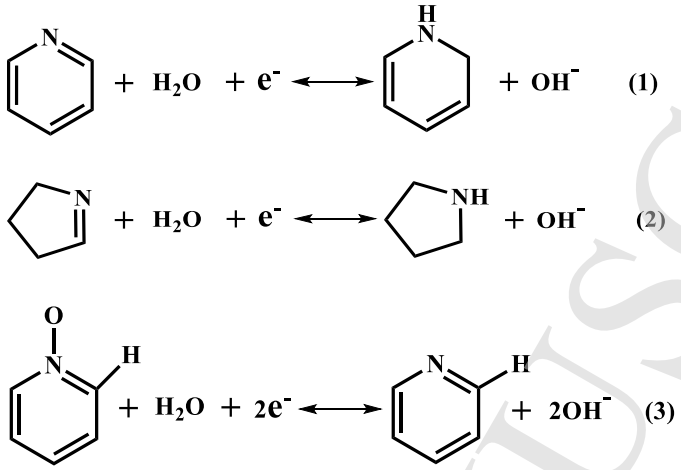

As for the F 1s spectrum of the ***Carbon-N-F*** sample, as revealed in Figure 4f, it is low-intensity and can be deconvoluted into two sub-bands, i.e., ionic C─F and semi-ionic C─F.[18,35] Additionally, the structural formula of nitrogen/fluorine groups in a graphitic structure is depicted in Figure 1. The atomic contents of C, N, O and F from XPS analysis are given in Table 2.

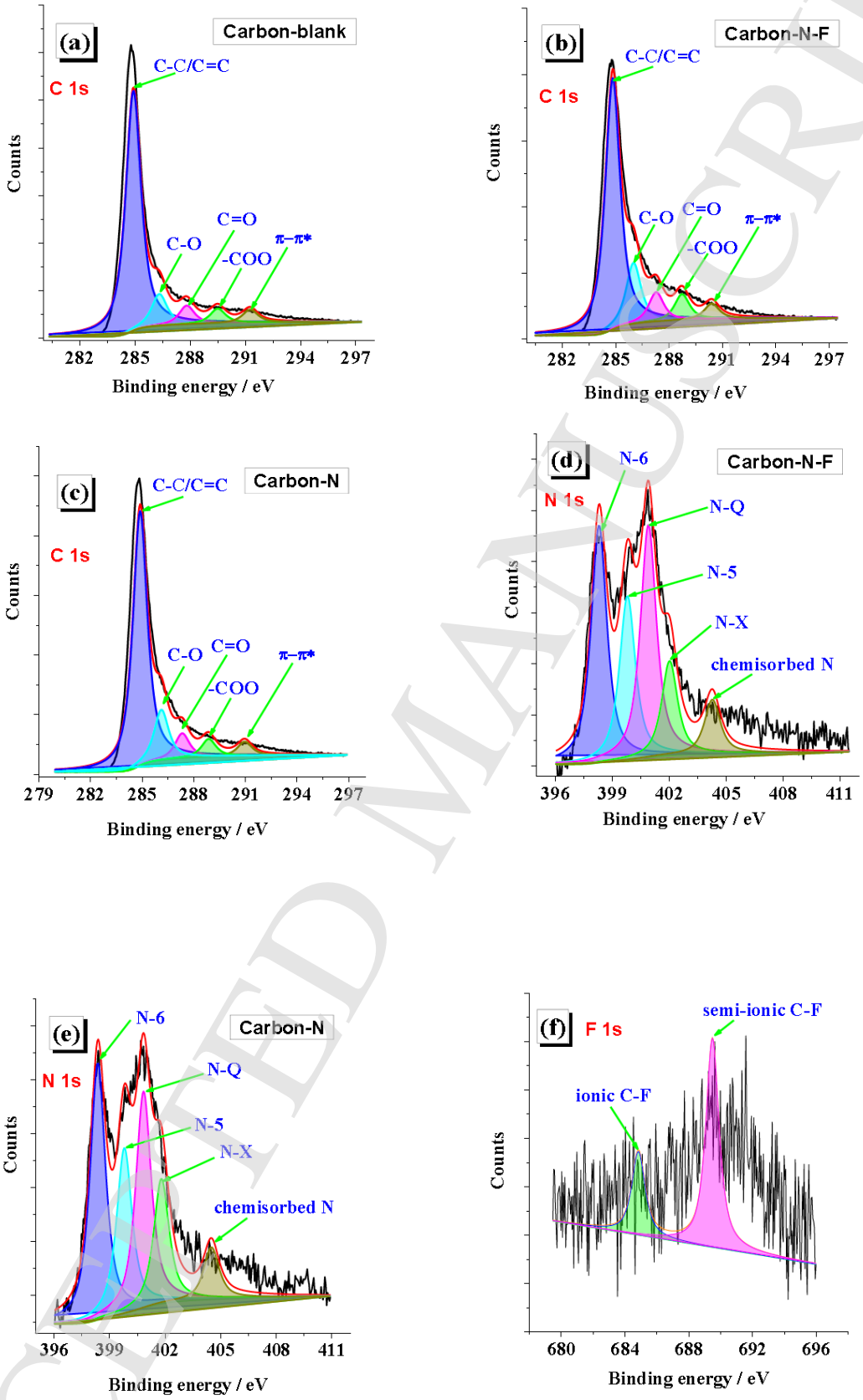

Figure 4. XPS of the ***Carbon-blank, Carbon-N-F, Carbon-N*** samples: (a-c) C 1s; (d-e) N 1s; (f) F 1s.

Table 2. The atomic contents of C, N, O and F from XPS analysis.

samples	C/at%	N/at%	O/at%	F/at%
Carbon-blank	93.59	/	6.41	/
Carbon-N-F	86.21	6.40	6.81	0.58
Carbon-N	85.89	7.58	6.53	/

HRTEM images, elemental mappings and EDAX spectrum were utilized to vividly depict the shapes, sizes and components of the ***Carbon-blank***, ***Carbon-N-F***, and ***Carbon-N*** samples. Figure 5 a, b have shown the typical HRTEM images of ***Carbon-blank*** sample, which are entirely composed of 2D PCNSs with the sizes of several hundreds of nanometers. And the existence of lots of wrinkles indicates the flexibility of these PCNSs. Obviously, directly carbonizing trisodium citrate at elevated temperatures leads to the formation of 2D PCNSs, really providing us an facile but effective approach, especially without extra template or activation agent.[20] The N and O elements of the ***Carbon-blank*** sample are well distributed and uniform, as shown in Figure 5 c, d, which are also supported by the EDAX spectrum in Figure 5 e.

When further heating trisodium citrate with ammonium fluoride at 800 °C, the resulting ***Carbon-N-F*** sample still displays 2D porous nanostructures, as shown in Figure 5 f, g, slightly different from the ***Carbon-blank*** sample. The corresponding elemental mappings and EDAX spectrum of C, O, N and F are depicted in Figure 5 h-l, in which the mapping of fluorine is relatively unambiguous, also indicating its low content of 0.58% (as given in Table 2). On the other hand, when heating trisodium citrate with ammonium chloride at 800 °C, the resultant ***Carbon-N*** sample compared to the ***Carbon-N-F*** sample exhibits similar HRTEM, elemental mappings and EDAX results, as shown in Figure 5 m-r. As for the 2D carbon nanostructures towards these samples, they were also evinced by FESEM results, as depicted in Figure S2.

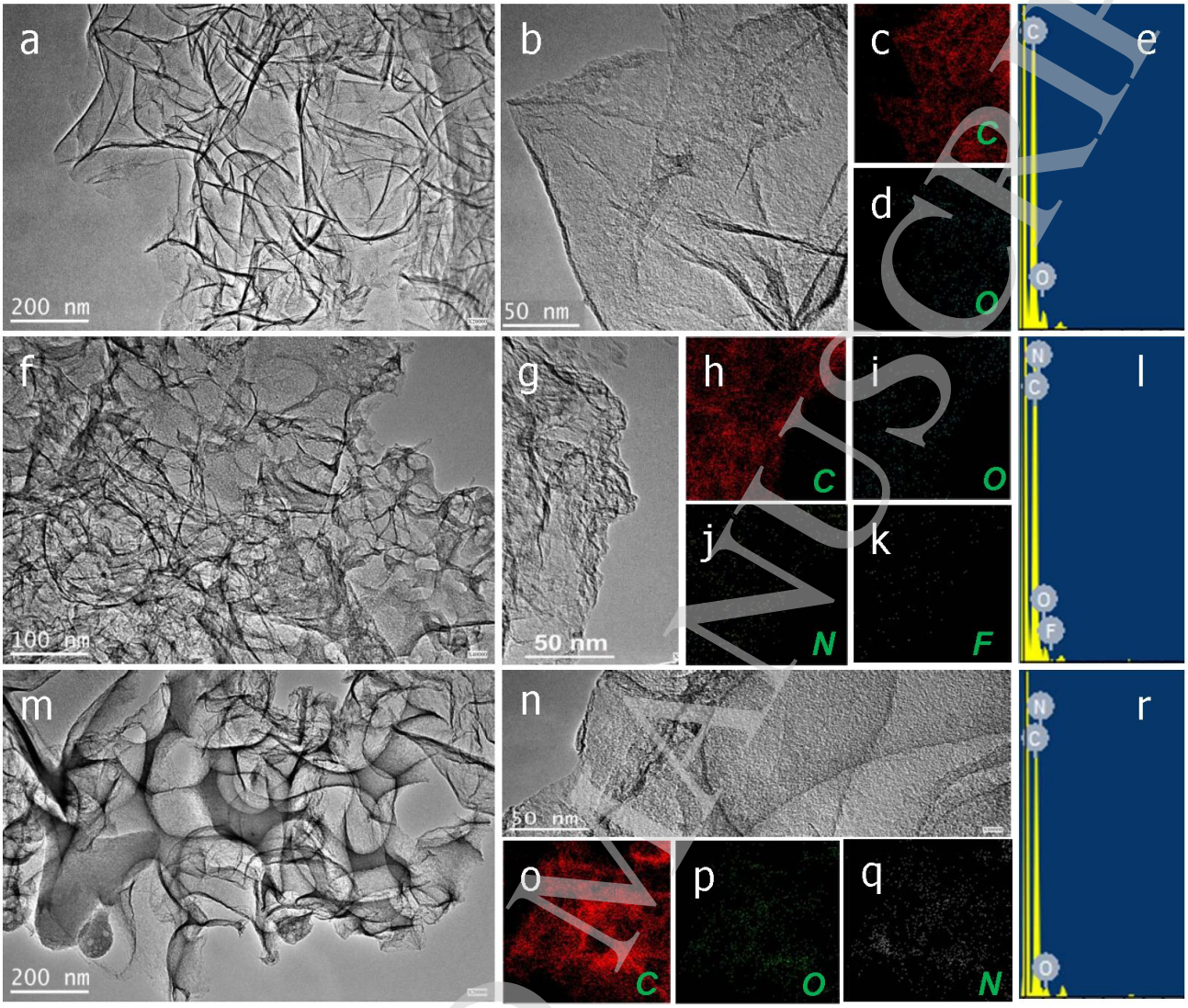

Figure 5. HRTEM images, elemental mappings and EDAX spectra: (a-e) ***Carbon-blank***; (f-l) ***Carbon-N-F***; (m-r) ***Carbon-N***.

3.2 Electrochemical measurements

Electrochemical performances of the as-obtained ***Carbon-blank, Carbon-N-F, and Carbon-N*** samples were tested in a three-electrode system, using 1 mol L^{-1} H_2SO_4 solution as aqueous electrolyte. Figure 6a indicates the serial CV curves of the ***Carbon-blank*** sample with the scan rates from 10 to 100 mV s^{-1}, and their outlines are quite close to rectangle in the potential scope of 0 ~ 1 V. It clearly reveals that electric double layer capacitances (EDLCs) contribution is fairly predominant for the whole capacitance towards the ***Carbon-blank*** sample.[36] This kind of EDLCs feature is also validated by the GCD curves showing nearly triangular shapes in Figure 6b.

Next, for the sake of investigating the capacitive behaviors of the ***Carbon-blank***, ***Carbon-N-F***, and ***Carbon-N*** samples, we designated the scan rate at 30 mV s^{-1}, and the resulting CV profiles are displayed in Figure 6c. It is apparent to us that, from the viewpoint of integrate CV area, the ***Carbon-N-F*** sample exhibits the largest one whilst the pristine ***Carbon-blank*** sample shows the minimum case. Considering the fact that specific capacitance is usually proportional to the integrate CV area, we can therefore conclude that the specific capacitance order between these samples is as follows: ***Carbon-N-F*** > ***Carbon-N*** > ***Carbon-blank***. And similar variation tendency also occurs for the case of GCD results, as demonstrated in Figure 6d.

As a result, in terms of specific capacitance from GCD curves, the ***Carbon-N-F*** sample delivers much larger capacitances that those of the other samples at the current density of 1 ~ 10 A g^{-1}, as given in Figure 6e. For example, the ***Carbon-N-F*** sample shows specific capacitance of 169 F g^{-1}, whereas those of the ***Carbon-N***, ***Carbon-blank*** samples are of 78 and 49 F g^{-1} at 1A g^{-1}. Besides, energy efficiency and rate capability are also crucial for determining the capacitive behaviors of supercapacitors. In present work, we thereby calculated the above two factors, as shown in Figure 6f. Distinctly, the ***Carbon-blank*** sample possesses the highest energy efficiency and rate capability among them. In brief, in a three-electrode system using 1 mol L^{-1} H_2SO_4 solution as electrolyte, the incorporation of N/F species producing additional pseudocapacitance within carbon matrix is favorable of acquiring larger total capacitance but accompanying with the deterioration of energy efficiency and rate capability, just like the behavior of redox additive of *p*-phenylenediamine in KOH electrolyte.[37]

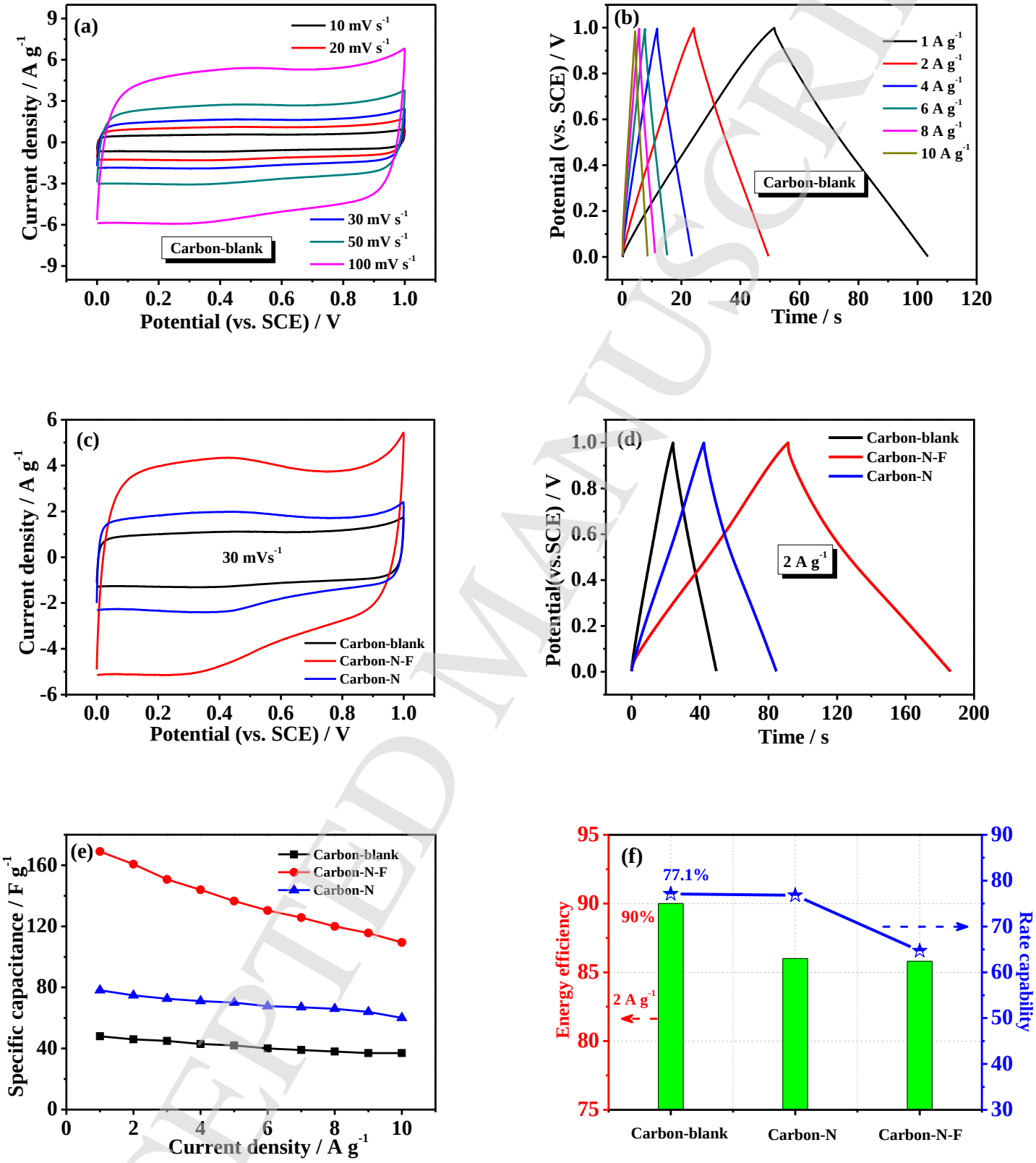

Figure 6. Electrochemical performance of the ***Carbon-blank, Carbon-N-F, Carbon-N*** samples tested in a three-electrode system: (a, c) CV curves; (b, d) GCD curves; (e)

Specific capacitance versus current density; (f) Energy efficiency and rate capability.

Next, electrochemical performance of the ***Carbon-blank***, ***Carbon-N-F***, and ***Carbon-N*** samples was tested in a two-electrode system. Figure 7 a, b show the contrast CV curves and GCD curves, respectively, which are almost the same as those obtained in three-electrode system (in Figure 6 c, d), but accompanying with the decrease of discharging time. This is caused by the fact that two-electrode configuration test is more accurate that three-electrode one.[38] Analogously, the specific capacitances of the ***Carbon-blank***, ***Carbon-N-F***, and ***Carbon-N*** samples are of 28, 110, and 46 F g^{-1} at 1A g^{-1}, respectively. In any case, the ***Carbon-N-F*** sample delivers the largest capacitance mostly because semi-ionic C–F bonds in PCNSs have enhanced electrical conductivity and hence facilitated electron transport in the electrode.[39-41] As for cycling stability, it was also measured towards the three samples and the results are shown in Figure 7d.

Ragone plot shows a chart of specific energy (how much energy is available) versus specific power (how quickly that energy can be delivered). By calculation, the energy/power densities of the ***Carbon-blank***, ***Carbon-N-F***, and ***Carbon-N*** samples are given in Figure 7e. At the power density of 0.5 kW kg^{-1}, the ***Carbon-N-F*** sample exhibits the largest energy density of 3.82 W h kg^{-1}, much larger than the others. Clearly, the incorporation of N/F and porosity both exerts major roles in determining the eventual capacitive performances, and the synergisitic effect of N and F doping makes the improvement of energy density towards the present carbon materials.

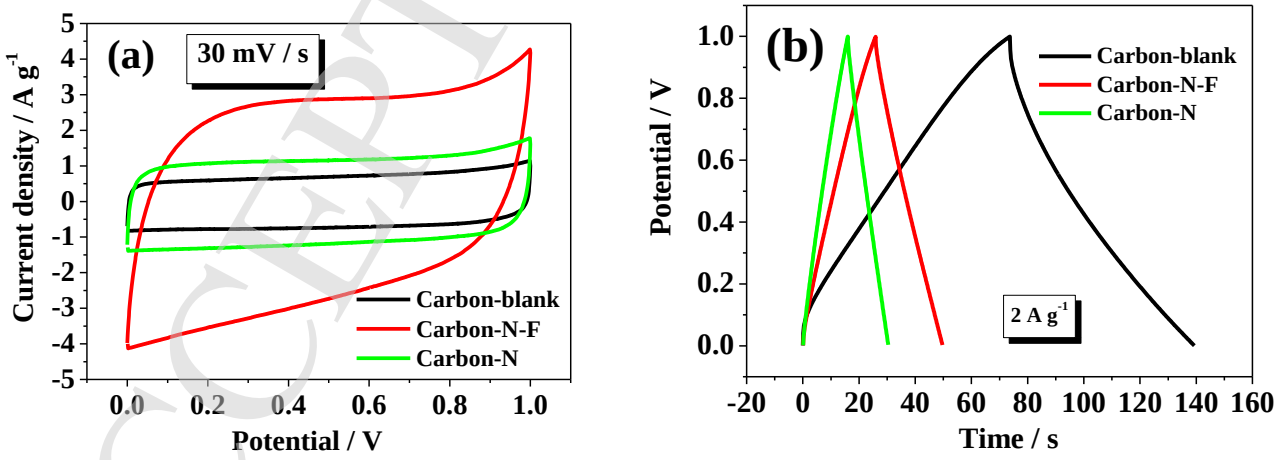

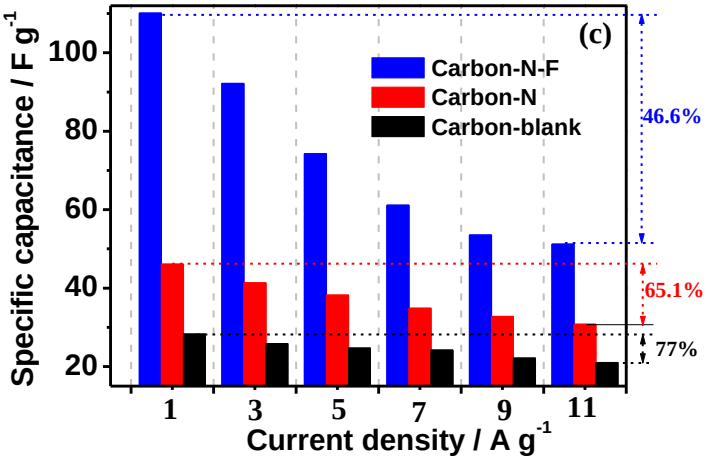

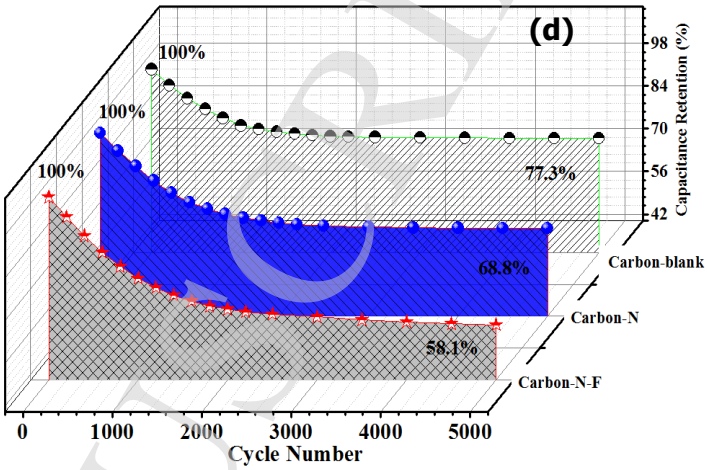

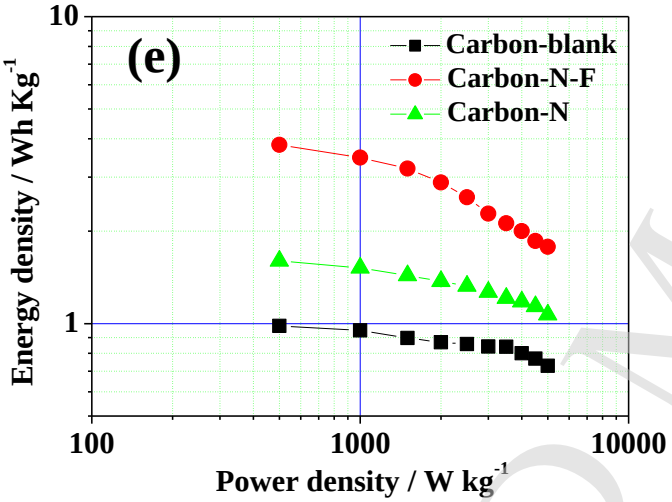

Figure 7. Electrochemical performance of the ***Carbon-blank, Carbon-N-F, Carbon-N*** samples tested in a two-electrode system: (a) CV curves; (b) GCD curves; (c) Specific capacitance versus current density; (d) Cycling stability; (e) Ragone plots.

Nyquist plot, also known as electrochemical impedance spectroscopy (EIS), shows the frequency response of the electrode/electrolyte system and the imaginary part of the impedance is plotted as a function of the real part, often represented as follows [42]:

$$Z = \frac{E}{I} = Z_0 \exp(j\phi) = Z_0(\cos\phi + j\sin\phi) \qquad (7)$$

For an ideal capacitor, the Nyquist plot would show a vertical line only coinciding with the vertical axis with the real part of Z being 0.

Figure 7g displays the typical Nyquist plots of the ***Carbon-blank***, ***Carbon-N-F***, and ***Carbon-N*** samples. As is well known, the vertical shape at lower frequencies indicates a pure capacitive behavior, representative of the ion diffusion in the structure of the electrode [43]. Therefore, it is seen from Figure 7g that the ***Carbon-N-F***, and ***Carbon-N*** samples show more vertical shapes than the ***Carbon-blank*** at lower frequencies; and also, the equivalent series resistances among them also indicates the same tendency, judged by the *x*-intercept of the inset of Figure 7g. Clearly, the above reveals the role of N/F incorporation into carbon.

Furthermore, the relation of the imaginary part (C″) of the capacitance versus frequency is demonstrated in Figure 8b. The plots of all samples go through a maximum at a particular frequency (f_k). This frequency determines the dielectric relaxation time (τ), which can be acquired by following equation: $\tau = 1/f_k$ [44]. As we know, smaller value represents shorter time for the supercapacitor to reach half of the low frequency capacitance, implying the better power properties of the system [45]. As a result, the C″ of the ***Carbon-N-F*** sample exhibits a maximum with the particular frequency of 0.67 Hz, and the corresponding relaxation time is of 1.5 s. It is much lower than the ones of the ***Carbon-blank*** and ***Carbon-N*** samples. Meanwhile, similar variation tendency also occurs for the case of real part of capacitance versus frequency in Figure 8c.

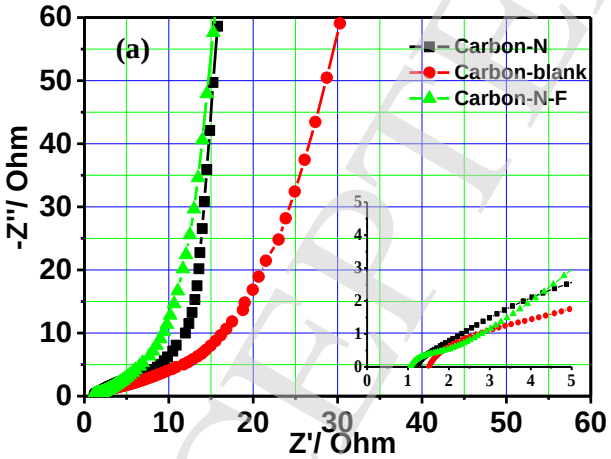

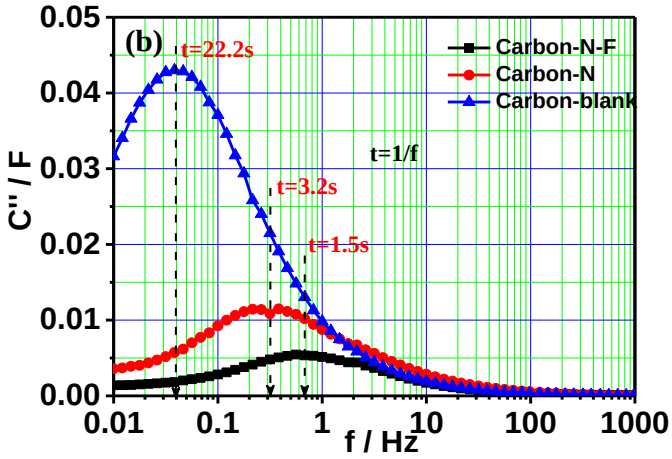

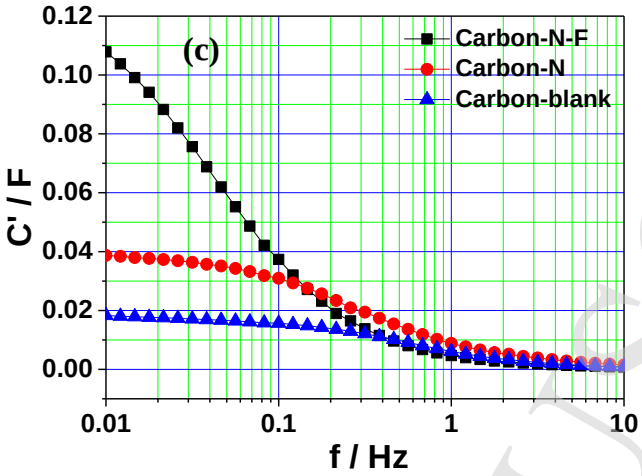

Figure 8. Electrochemical performance of the ***Carbon-blank***, ***Carbon-N-F***, ***Carbon-N*** samples tested in a two-electrode system: (a) Nyquist plots; and evolution of (b) imaginary and (c) real part of capacitance versus frequency.

4. Conclusions

In summary, in a comparative manner, ammonium fluoride and ammonium chloride are utilized as efficient dopants for producing N/F-doped carbon materials. The as-obtained carbon samples have been characterized by XRD, Raman, XPS, BET&PSD, and HRTEM for structure analysis, and also measured in a three-electrode system and two-electrode system, respectively. Most noteworthy, the electrochemical measurements has revealed that the dual incorporation of N/F species producing additional pseudocapacitance within carbon matrix is favorable of acquiring larger total capacitance, higher energy density but accompanying with the slight deterioration of energy efficiency, cycling stability and rate capability. In brief, the present co-incorporation of N/F into carbon provides a facile but efficient avenue for producing high-energy density supercapacitors.

Acknowledgments

Financial supports from National Natural Science Foundation of China (51602003), Startup Foundation for Doctors of Anhui University (J01003211), and

Key Research and Development Projects of Anhui in 2018 (1804a09020064) are greatfully acknowledged.

References

1. X. Zheng, J. Luo, W. Lv, D. W. Wang and Q. H. Yang, (2015) DOI: 10.1002/adma.201501452.
2. Z. J. Zhang, Q. C. Zheng, L. Sun, D. Xu and X. Y. Chen, *Ind. Eng. Chem. Res*. **56**, 12344 (2017).
3. D. Xu, W. Hu, X. N. Sun, P. Cui and X. Y. Chen, *J. Power Sources* **341**, 448 (2017).
4. H. Fan and W. Shen, *ChemSusChem* **8**, 2004 (2015).
5. H. Nishihara and T. Kyotani, *Adv. Mater.* **24**, 4473 (2012).
6. W. Hu, D. Xu, X. N. Sun, Z. H. Xiao, X. Y. Chen and Z. J. Zhang, *ACS Sus. Chem. Eng.* **5**, 8630 (2017).
7. D. Xu, X. N. Sun, W. Hu and X. Y. Chen, *J. Power Sources* **357**, 107 (2017).
8. X. N. Sun, D. Xu, W. Hu and X. Y. Chen, *ACS Sus. Chem. Eng.* **5**, 5972 (2017).
9. J. P. Paraknowitsch and A. Thomas, *Energy Environ. Sci*. **6**, 2839 (2013).
10. M. Yang and Z. Zhou, *Adv. Sci*. (2017) DOI: 10.1002/advs.201600408.
11. W. Shen and W. Fan, *J. Mater. Chem. A* **1**, 999 (2013).
12. Y. F. Nie, Q. Wang, X. Y. Chen and Z. J. Zhang, *J. Power Sources* 320, 140 (2016).
13. P. Wang, B. Qiao, Y. Du, Y. Li, X. Zhou, Z. Dai and J. Bao, *J. Phys. Chem. C* **119**, 21336 (2015).
14. H. An, Y. Li, Y. Gao, C. Cao, J. Han, Y. Feng and W. Feng, *Carbon* **116**, 338 (2017).
15. X. Yue, S.Huang, Y. Jin and P. K. Shen, *Catal. Sci. Technol*. **7**, 2228 (2017).
16. S. Fu, C. Zhu, J. Song, M. H. Engelhard, B. Xiao, D. Du and Y. Lin, *Chem. Eur. J.* **23**, 10460 (2017).
17. J. Zhou, J. Lian, L. Hou, J. Zhang, H. Gou, M. Xia, Y. Zhao, T. A. Strobel, L. Tao and D. Gao, *Nat. Commun*. **6**, 8503 (2015).
18. W. Na, J. Jun, J. W. Park, G. Lee and J. Jang, *J. Mater. Chem. A* **5**, 17379 (2017).
19. J. Kim, J. Chun, S. G. Kim, H. Ahn and K. C. Roh, *J. Electrochem. Sci. Technol*. **8**, 338 (2017).
20. Q. Wang, Y. F. Nie, X. Y. Chen, Z. H. Xia and Z. J. Zhang, *Electrochim. Acta* **200**, 247 (2016).

21. Y. Zhu, T. Cao, C. Cao, X. Ma, X. Xu and Y. Li, *Nano Res*. **11**, 3088 (2018).
22. Y. Wang, D. C. Alsmeyer and R. L. McCreery, *Chem. Mater*. **2**, 557 (1990).
23. B. Krüner, A. Schreiber, A. Tolosa, A. Quade, F. Badaczewski, T. Pfaff, B. M. Smarsly and V. Presser, *Carbon* **132**, 220 (2008).
24. A. Sadezky, H. Muckenhuber, H. Grothe, R. Niessner and U. Pöschil, *Carbon* **43**, 1731 (2005).
25. F. Tuinstra and J. L. Koenig, *J. Chem. Phys*. **53**, 1126 (1970).
26. P. K. Chu and L. Li, *Mater. Chem. Phys*. **96**, 253 (2006).
27. Z. Qiu, Y. Wang, X. Bi, T. Zhou, J. Zhou, J. Zhao, Z. Miao, W. Yi, P. Fu and S. Zhuo, *J. Power Sources* **376**, 82 (2018).
28. X. Y. Chen, C. Chen, Z. J. Zhang and D. H. Xie, *J. Mater. Chem. A* **1**, 14919 (2013).
29. Y. P. Zhai, Y. Q. Dou, D. Y. Zhao P. F., Fulvio, R. T. Mayes and S. Dai, *Adv. Mater*. **23**, 4828 (2011).
30. W. Shen, Z. Li and Y. Liu, *Recent Patents Chem. Eng.* **1**, 27 (2008).
31. T. I. T. Okpalugo, P. Papakonstantinou, H. Murphy, J. McLanghlin and N. M. D. Brown, *Carbon* **43**, 153 (2005).
32. V. Datsyuk, M. Kalyva, K. Papagelis, J. Parthenios, D. Tasis, A. Siokou, I. Kallitsis and C. Galiotis, *Carbon* **46**, 833 (2008).
33. D. W. Wang, F. Li, L. C. Yin, X. Lu, Z. G. Chen, I. R. Gentle, G. Q. Lu and H. M. Cheng, *Chem. Eur. J*. **18**, 5345 (2012).
34. K. N. Wood, R. O'Hayre and S. Pylypenko, *Energy Environ. Sci*. **7**, 1212 (2014).
35. H. An, Y. Li, P. Long, Y. Gao, C. Qin, C. Cao, Y. Feng and W. Feng, *J. Power Sources* **312**, 146 (2016).
36. M. Sevilla and A. B. Fuertes, *ACS Nano* **8**, 5069 (2014).
37. Z. J. Zhang and X. Y. Chen, *J. Electroanal. Chem*. **764**, 45 (2016).
38. M. D. Stoller, S. Park, Y. Zhu, J. An and R. S. Ruoff, *Nano Lett.* **8**, 3498 (2008).
39. Y. Geng, Y. Song, M. Zhong, J. Shi, Q. Guo and L. Liu, *Mater. Lett*. **64**, 2673 (2010).
40. E. Jeong, M. J. Jung, S. G. Lee, H. G. Kim and Y. S. Lee, *J. Ind. Eng. Chem*. **43**, 78 (2016).
41. S. M. Li and C. C. Hu, *J. Power Sources* **278**, 218 (2015).
42. R. Kötz, M. Hahn and R. Gallay, *J. Power Sources* **154**, 550 (2006).
43. Y. Wang, C. Wang and Y. Chen, *J. Phys. Chem. C* **113**, 13103 (2009).

44. E. Y. L. Teo and K. F. Chong, *Electrochim. Acta* **192**, 110 (2016).

45. P. Sivaraman, K. Shashidhara and A. B. Samui, *Electrochim. Acta* 55, 2451 (2010).